Pacific Northwest
NATIONAL LABORATORY

PNNL-38914

Model Parameter Development for Complex Materials

Species-Specific Diffusion Barriers in 316 Stainless Steel from Systematic DFT Calculations

January 2026

Erin I Barker
Scott E Muller
Floyd W Hilty
Kathy Nwe
Julia H Nguyen
Manny Bonilla

U.S. DEPARTMENT of ENERGY

Prepared for the U.S. Department of Energy
under Contract DE-AC05-76RL01830

DISCLAIMER

PACIFIC NORTHWEST NATIONAL LABORATORY
operated by
BATTELLE
for the
UNITED STATES DEPARTMENT OF ENERGY
under Contract DE-AC05-76RL01830

Printed in the United States of America

Available to DOE and DOE contractors from
the Office of Scientific and Technical Information,
P.O. Box 62, Oak Ridge, TN 37831-0062
www.osti.gov
ph: (865) 576-8401
fox: (865) 576-5728
email: reports@osti.gov

Available to the public from the National Technical Information Service
5301 Shawnee Rd., Alexandria, VA 22312
ph: (800) 553-NTIS (6847)
or (703) 605-6000
email: info@ntis.gov
Online ordering: http://www.ntis.gov

PNNL-38914

Model Parameter Development for Complex Materials

Species-Specific Diffusion Barriers in 316 Stainless Steel from Systematic DFT Calculations

January 2026

Erin I Barker
Scott E Muller
Floyd W Hilty
Kathy Nwe
Julia H Nguyen
Manny Bonilla

Prepared for
the U.S. Department of Energy
under Contract DE-AC05-76RL01830

Pacific Northwest National Laboratory
Richland, Washington 99354

Abstract

Vacancy-mediated diffusion barriers in 316 stainless steel have been systematically calculated using density functional theory to provide essential parameters for mesoscale microstructure evolution models. A statistical sampling approach employing 210 nudged elastic band calculations across multiple special quasi-random structures captures the effects of local chemical environments in this concentrated alloy. The computational methodology addresses challenges specific to chemically disordered systems, including proper magnetic treatment throughout multi-step calculations and validation against experimental structural properties. The calculated activation barriers reveal clear species-dependent diffusion behavior with the hierarchy Ni >> Fe ≈ Cr >> Mo. Nickel exhibits the highest barriers (0.74–1.31 eV, mean 1.045 eV), confirming its role as the slowest-diffusing major component. Iron and chromium show similar moderate barriers averaging 0.587 eV and 0.522 eV, respectively. Remarkably, molybdenum demonstrates exceptionally low barriers (0.12–0.28 eV, mean 0.194 eV), suggesting much higher mobility than previously recognized and potentially significant implications for precipitation kinetics and microstructure evolution. The barrier ranges remain consistent across different 316 SS compositions, supporting parameter transferability for modeling applications. The overall mean barrier of 0.64 eV provides a practical approximation for phase field simulations, while species-specific values enable detailed treatments of diffusion-controlled processes. This systematic approach establishes a validated framework for generating diffusion parameters in other concentrated alloys where experimental data are limited, while providing the first systematic set of species-specific barriers for predictive modeling of 316 stainless steel microstructure evolution.

Summary

This report outlines the vacancy-mediated diffusion behavior in 316 stainless steel through the systematic application of density functional theory (DFT). The findings clarify species-specific diffusion barriers, revealing the intrinsic hierarchy (Ni >> Fe ~ Cr >> Mo), with Mo demonstrating exceptional mobility. These results have implications beyond understanding basic alloy diffusion—Ni acts as the rate-limiting species, while Mo's rapid redistribution could critically impact microstructure stability and precipitation kinetics during thermal processing. The overall mean barrier of 0.64 eV offers a simplified parameter for phase field simulations, transferable to modeling other concentrated alloys, while species-specific values enable more nuanced analyses of diffusion-controlled phenomena. This validated computational methodology provides a pathway for generating quantitative parameters essential for predictive modeling in complex alloys, addressing gaps where experimental data are unavailable or insufficient.

Acknowledgments

This research was supported by the Generative Artificial Intelligence Initiative, under the Laboratory Directed Research and Development (LDRD) Program at Pacific Northwest National Laboratory (PNNL). PNNL is a multi-program national laboratory operated for the U.S. Department of Energy (DOE) by Battelle Memorial Institute under Contract No. DE-AC05-76RL01830. Research was performed using resources available through Research Computing at PNNL.

Acronyms and Abbreviations

PNNL – Pacific Northwest National Laboratory

DOE – U.S. Department of Energy

LDRD – Laboratory Directed Research and Development

DFT – Density Functional Theory

NEB – Nudged Elastic Band

ENCUT – Plane-wave energy cutoff

PAW – Projector Augmented Wave

FCC – Face-Centered Cubic

SS – Stainless Steel

SQS – Special Quasi-random Structures

Contents

Figures

1.0 Introduction

Atomic diffusion in austenitic stainless steels controls microstructural evolution during high-temperature service, affecting mechanical properties, creep resistance, and radiation tolerance (Li et al. 2017). Understanding diffusion kinetics at the atomic scale provides essential input parameters for mesoscale modeling approaches such as phase field simulations of precipitate evolution and crystal plasticity models of deformation behavior (Liu, Li, and Zhan 2018). While experimental measurements of diffusion in stainless steels provide macroscopic activation energies, they typically cannot resolve the individual contributions of different atomic species or capture the effects of local chemical environments in these multicomponent alloys (e.g., composition fluctuations, local solute clustering) (Ponga et al. 2022).

Experimental studies of diffusion in 300-series stainless steels report overall activation energies for bulk diffusion on the order of 1–3 eV (Arunkumar et al. 2009; Assassa and Guiraldenq 1978). Simultaneous tracer measurements of 59Fe, 51Cr, and 63Ni in austenitic Fe–Cr–Ni alloys consistently show a hierarchy of diffusivities with DCr > DFe > DNi, indicating that Ni has the highest activation barrier and is the slowest bulk diffuser among the major constituents (Assassa and Guiraldenq 1978; Rothman, Nowicki, and Murch 1980). Reported activation enthalpies for these species typically lie in the range of ~240–290 kJ/mol (2.5–3.0 eV), with Cr near the lower end and Ni near the upper end of this range (Rothman, Nowicki, and Murch 1980; Assassa and Guiraldenq 1978). These measurements represent the combined effect of vacancy formation and migration energies and average over the range of local chemical environments present in the alloy (Mehrer 2007). While valuable for engineering applications, these macroscopic parameters provide limited insight into the atomic-scale mechanisms governing diffusion in chemically complex alloys.

Density functional theory (DFT) calculations have provided detailed information about vacancy-mediated diffusion in simpler Fe-Cr-Ni systems, typically finding migration barriers on the order of ~1 eV for nearest-neighbor hops, with species-specific differences (Ni >> Fe ≈ Cr) (Fisher et al. 2025; Klaver, Hepburn, and Ackland 2012). For example, Klaver et al. report barrier ranges in austenite of ~0.6–1.3 eV for migration in dilute Fe-Cr-Ni systems (Klaver, Hepburn, and Ackland 2012). However, systematic DFT studies of diffusion barriers in full 316 stainless steel compositions, including the effects of molybdenum, remain limited (to our knowledge).

The challenge lies in properly accounting for the chemical disorder inherent in these concentrated alloys, where local atomic environments vary significantly from site to site (i.e., a given jump path may see different neighbor configurations, different local strains or magnetic states (Ponga et al. 2022; Xi et al. 2022). Xi et al. systematically demonstrated how local lattice distortions lead to large variations in vacancy migration barriers in FCC alloys (Xi et al. 2022), motivating the need for statistical sampling approaches such as those developed in this work.

Calculating diffusion barriers in chemically disordered alloys requires careful attention to statistical sampling and computational methodology. The nudged elastic band (NEB) method for finding minimum energy pathways can produce unphysical results in complex chemical environments if proper precautions are not taken, particularly regarding path initialization and the number of intermediate images used in the calculation (Henkelman and Jónsson 2000).

This work presents a systematic approach for calculating vacancy-mediated diffusion barriers in 316 stainless steel using DFT methods. We develop a workflow that addresses the challenges of chemical disorder through statistical sampling across multiple structural arrangements and provide species-specific diffusion parameters for Fe, Cr, Ni, and Mo atoms. The methodology

emphasizes best practices for NEB calculations in complex alloys and generates quantitative parameters suitable for input into mesoscale diffusion models.

2.0 Methods

2.1 DFT Setup and Convergence Testing

All calculations were performed using the Vienna Ab initio Simulation Package (VASP) (Georg et al. 1996; Kresse and Joubert 1999) with projector augmented wave (PAW) pseudopotentials (Kresse and Joubert 1999) and the PBE exchange-correlation functional (Perdew, Burke, and Ernzerhof 1996). The pseudopotentials used were PAW_PBE Cr (06Sep2000), PAW_PBE Fe (06Sep2000), PAW_PBE Ni (02Aug2007), and PAW_PBE Mo (08Apr2002).

Convergence testing was performed to establish optimal computational parameters. Results are summarized in Figure 1. The plane-wave kinetic energy cutoff was found to be sufficiently converged at ENCUT = 430 eV, achieving energy convergence within 0.1 meV/atom while maintaining computational efficiency. K-point sampling employed a 2×2×2 Monkhorst-Pack grid, providing convergence within 0.76 meV/atom for the 5×5×5 supercell (125 atoms). These choices represent a balance between accuracy and computational cost appropriate for the statistical sampling approach used in this study.

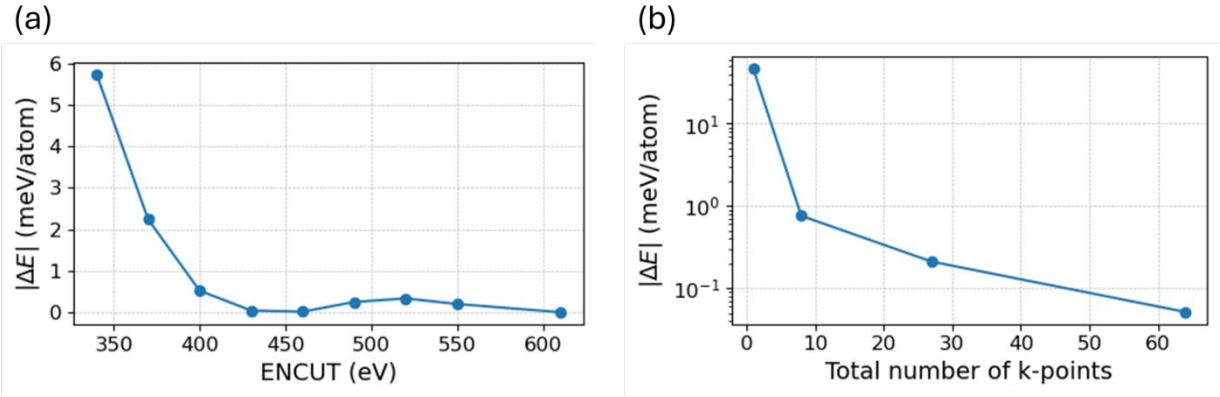

Figure 1. (a) Convergence of total energy per atom with respect to the plane-wave cutoff energy (ENCUT), reported relative to ENCUT = 610 eV. (b) Convergence of total energy per atom with respect to Brillouin-zone sampling, reported relative to the densest k-point mesh (5×5×5). The y-axis is shown on a logarithmic scale to highlight the convergence behavior across coarse and dense meshes.

2.2 Structure Generation

Realistic 316 stainless steel structures were generated using the special quasi-random structure (SQS) approach (Zunger et al. 1990) implemented in the icet package (Ångqvist et al. 2019). Two representative compositions within the 316 SS specification range were studied:

- Composition 1: (high Cr/Ni content)
  - Target: Cr: 0.18, Ni: 0.14, Mo: 0.02, Fe: 0.66
  - Achieved: Cr: 0.176 (n=22), Ni: 0.144 (n=18), Mo: 0.016 (n=2), Fe: 0.664 (n=83)
- Composition 2: (low Cr/Ni content)
  - Target: Cr: 0.16, Ni: 0.10, Mo: 0.02, Fe: 0.72

- Achieved: Cr: 0.16 (n=20), Ni: 0.096 (n=12), Mo: 0.024 (n=3), Fe: 0.72 (n=90)

SQS structure quality was assessed using correlation function metrics (Q, max_res, rms_res), with acceptable structures showing Q ≤ 0.070 and max_res ≤ 0.03. For each composition, approximately 20 different atomic arrangements were generated to provide statistical sampling of local chemical environments.

2.3 Bulk Structure Optimization

Each SQS structure underwent a two-stage relaxation process. First, a damped dynamics initialization (ALGO = Damped, TIME = 0.05) was performed for one ionic step (NSW = 1) with full cell relaxation (ISIF = 3) while writing wavefunction data (LWAVE = True). This was followed by full structural relaxation using the Fast algorithm (ALGO = Fast, ISTART = 1) for up to 150 ionic steps with continued cell relaxation. Initial magnetic moments were set to 4.0 μB for Fe, Cr, and Mo, and 2.0 μB for Ni, allowing the electronic structure to optimize during relaxation. Spin-polarized calculations (ISPIN = 2) were used throughout to properly account for the magnetic nature of these alloys. An example structure is shown in Figure 2, which also shows the simulation workflow.

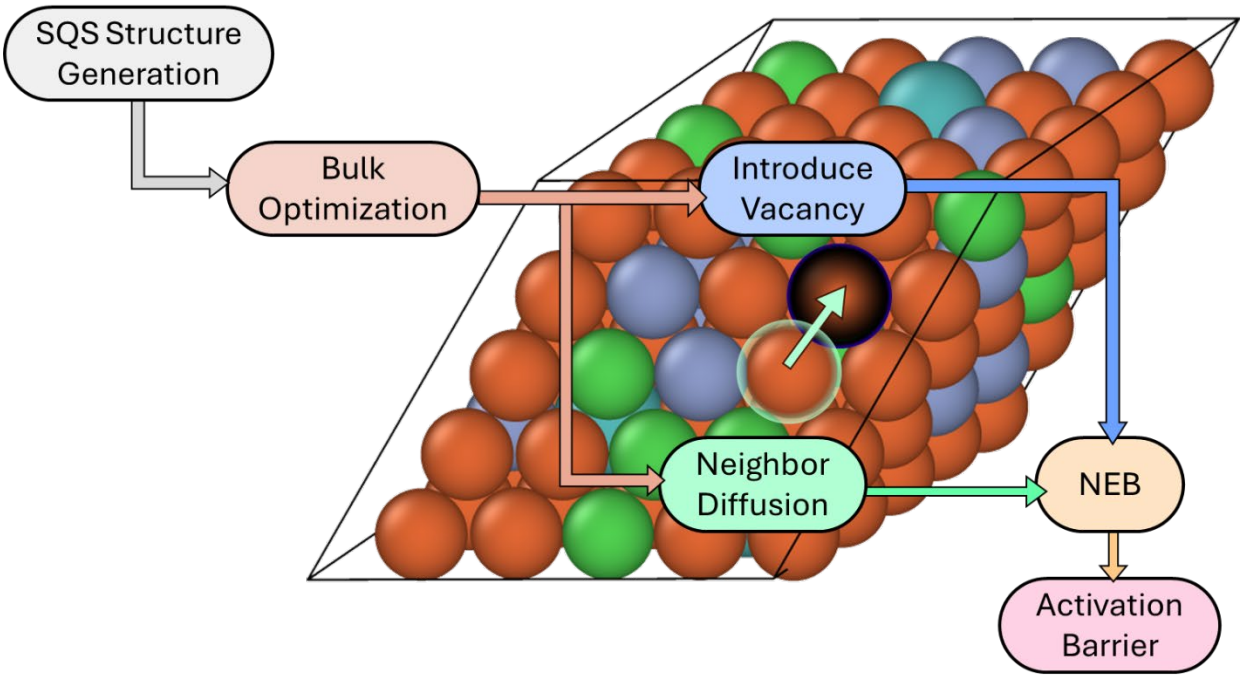

Figure 2. Example 316 SS simulation cell and workflow. Atomic structure visualization performed with OVITO (Stukowski 2009).

2.4 Computational Validation

The accuracy of the DFT setup was validated by computing the mass density of the optimized 316 SS structures, shown in Figure 3. Using the relaxed lattice parameters and atomic masses from the PAW pseudopotentials, calculated densities of 8.23 g/cm³ were obtained, representing a 2.8% deviation from the experimental density of 8.0 g/cm³ for 316 SS (Davis 1994). This level of agreement is typical for PBE-GGA calculations and confirms that the computational parameters provide a reasonable description of the structural properties of 316 stainless steel.

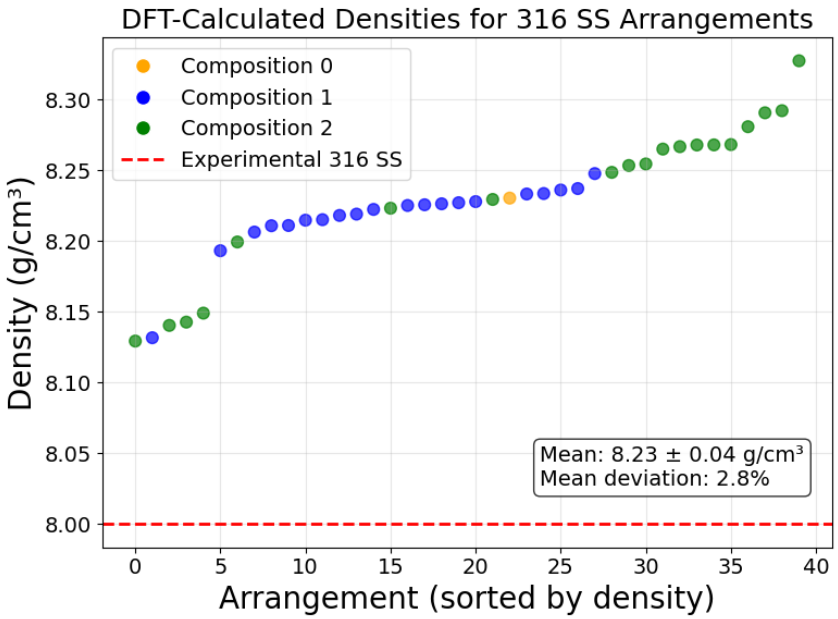

Figure 3. Density distribution of DFT-optimized 316 stainless steel structures across different atomic arrangements and compositions. Each point represents a fully relaxed 5×5×5 supercell (125 atoms) colored by composition variant: Composition 0 (orange), Composition 1 (blue), and Composition 2 (green). The horizontal dashed line indicates the experimental density of 316 SS (8.0 g/cm³). Arrangements are sorted by increasing density for clarity.

During the analysis, a small number of arrangements showing density deviations significantly outside the main distribution were identified as potential outliers. These structures, while sometimes exhibiting densities closer to the experimental value, produced activation barriers that deviated substantially from expected trends (e.g., Fe-Fe barriers exceeding typical Ni-Fe barriers). Such behavior suggests that these arrangements may have relaxed into unusual local minima that are not representative of typical 316 SS microstructures. There are five of these structures, seen on the lower left in the plot of Figure 3. These outlier arrangements were excluded from the barrier analysis to maintain statistical consistency, though their exclusion represents a conservative approach that may slightly bias results toward more common structural configurations.

2.5 Defect Creation and NEB Calculations

For each successfully relaxed bulk structure, approximately 10 vacancy-diffusion configurations were created by randomly selecting atom pairs for removal and diffusion. The diffusing atom was chosen from nearest neighbors to the vacancy site. Both initial and final defect structures were relaxed with atomic positions only (ISIF = 2) while maintaining the bulk lattice parameters, ensuring consistent reference states for barrier calculations.

Minimum energy pathways were calculated using the nudged elastic band (NEB) method (Henkelman, Uberuaga, and Jónsson 2000) with 3 intermediate images (5 total including endpoints). A test case with 9 intermediate images (11 total with endpoints) showed a 1.5% difference in activation barrier energy, indicating that 3 intermediate images are sufficient. The climbing image modification was employed (LCLIMB = True) to accurately locate transition states. Key NEB parameters included EDIFFG = -0.05 for force convergence, SPRING = -5 for

image coupling, and POTIM = 0.1 for ionic step control. Linear interpolation between relaxed initial and final states provided adequate initial path estimates for the FCC crystal structure.

2.6 Statistical Sampling and Analysis

From the planned 400 calculations (2 compositions × 20 arrangements × 10 defects), 28 bulk structures converged successfully, yielding 280 defect pairs plus 11 additional calculations from initial testing (composition 0). Of these, 267 successfully passed to the NEB stage, with 250 completing to the required accuracy. Of these, 40 were excluded from analysis due to their bulk structure having a significant density deviation from the average. The statistical sampling strategy thus generated a total of 210 NEB calculations across different local chemical environments. This sampling enables analysis of barrier distributions and species-specific effects while accounting for local chemical environment variations inherent in concentrated alloys.

2.7 Computational Best Practices

An important methodological consideration emerged during the work: consistent treatment of magnetic properties throughout the calculation workflow. All stages of the calculation, including NEB intermediate images, must use identical magnetic treatment (ISPIN = 2) to avoid artifacts. Initial testing with non-magnetic NEB calculations (ISPIN = 1) while using magnetic endpoints produced unphysically high barriers (~11 eV), which were corrected to physically reasonable values (~0.1–1.3 eV) upon implementing consistent magnetic treatment. This highlights the importance of maintaining electronic structure consistency throughout multi-step calculations in magnetic alloys.

3.0 Results and Discussion

3.1 Activation Barrier Distributions

A total of 210 vacancy-mediated diffusion barriers have been calculated across different local chemical environments in 316 stainless steel, including data from three compositional variants (11 calculations from composition 0, 150 from composition 1, and 49 from composition 2). The activation barriers range from 0.12 to 1.31 eV, with an overall mean of 0.64 eV. This range falls within the expected values for vacancy migration in FCC metals and alloys, confirming that the computational approach produces physically reasonable results.

The wide range of calculated barriers reflects both local chemical environment variations and intrinsic differences between diffusing species. Figure 4 illustrates representative examples of this species-dependent behavior through energy profiles calculated within a single atomic arrangement, effectively controlling for local environment effects. The four pathways show distinct barrier heights that span nearly an order of magnitude, from exceptionally low Mo barriers (~0.1 eV) to high Ni barriers (~1.2 eV), with Fe and Cr exhibiting intermediate values. This systematic variation suggests that diffusing species identity plays a central role in controlling vacancy-mediated transport in 316 stainless steel.

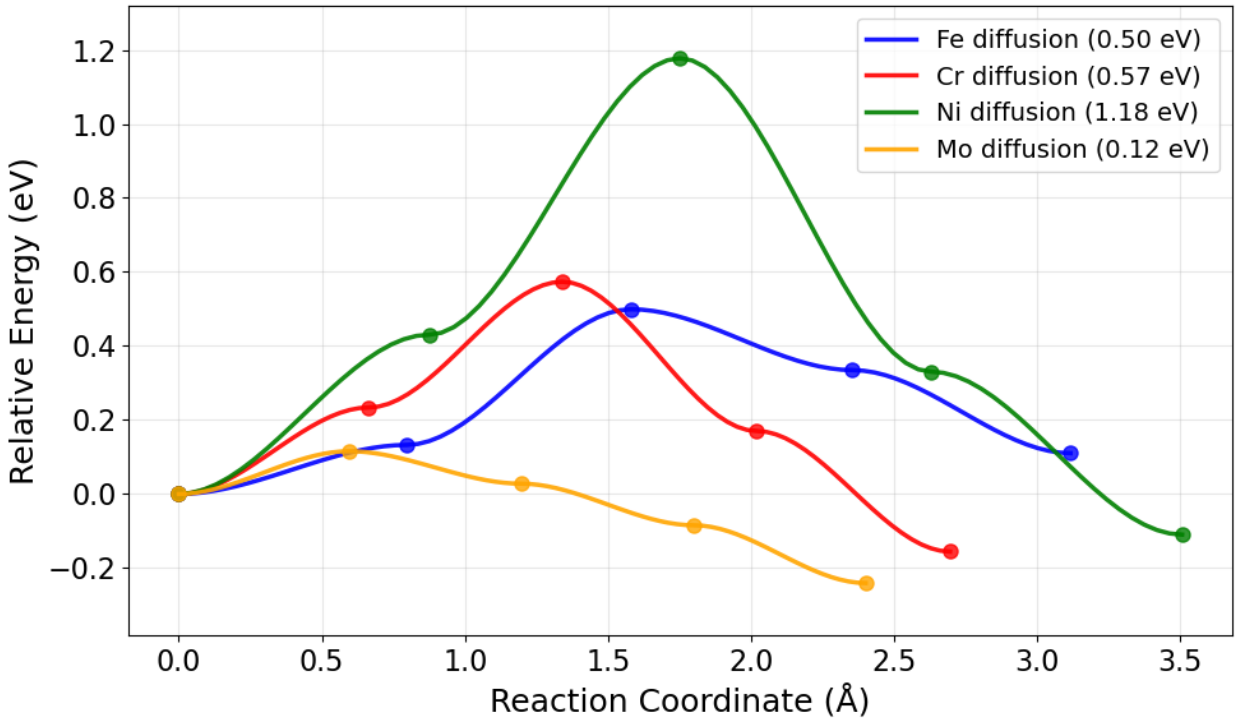

Figure 4. Representative nudged elastic band energy profiles for different diffusing species from a single atomic arrangement, demonstrating species-dependent diffusion behavior in 316 stainless steel. All four diffusion pathways originate from the same special quasi-random structure (one of the arrangements from Composition 1), controlling for local chemical environment effects. The energy profiles reveal distinct activation barriers: Mo (0.12 eV), Fe (0.50 eV), Cr (0.57 eV), and Ni (1.18 eV). Points indicate calculated NEB images, while lines show splined interpolations. All energies are referenced to their respective initial states.

The statistical analysis of all 210 calculations, shown in Figure 5, confirms the species-specific trends observed in the representative examples. The sorted distribution reveals clear separation between Mo and Ni, with significant overlap between Fe and Cr barriers. Within each species category, scatter reflects local chemical environment effects, validating the statistical sampling approach for concentrated alloys. The box plots establish a definitive hierarchy spanning nearly an order of magnitude, with mean barriers differing by factors of 2–5 between species. This systematic variation provides the foundation for examining the diffusion behavior of each alloying element in detail.

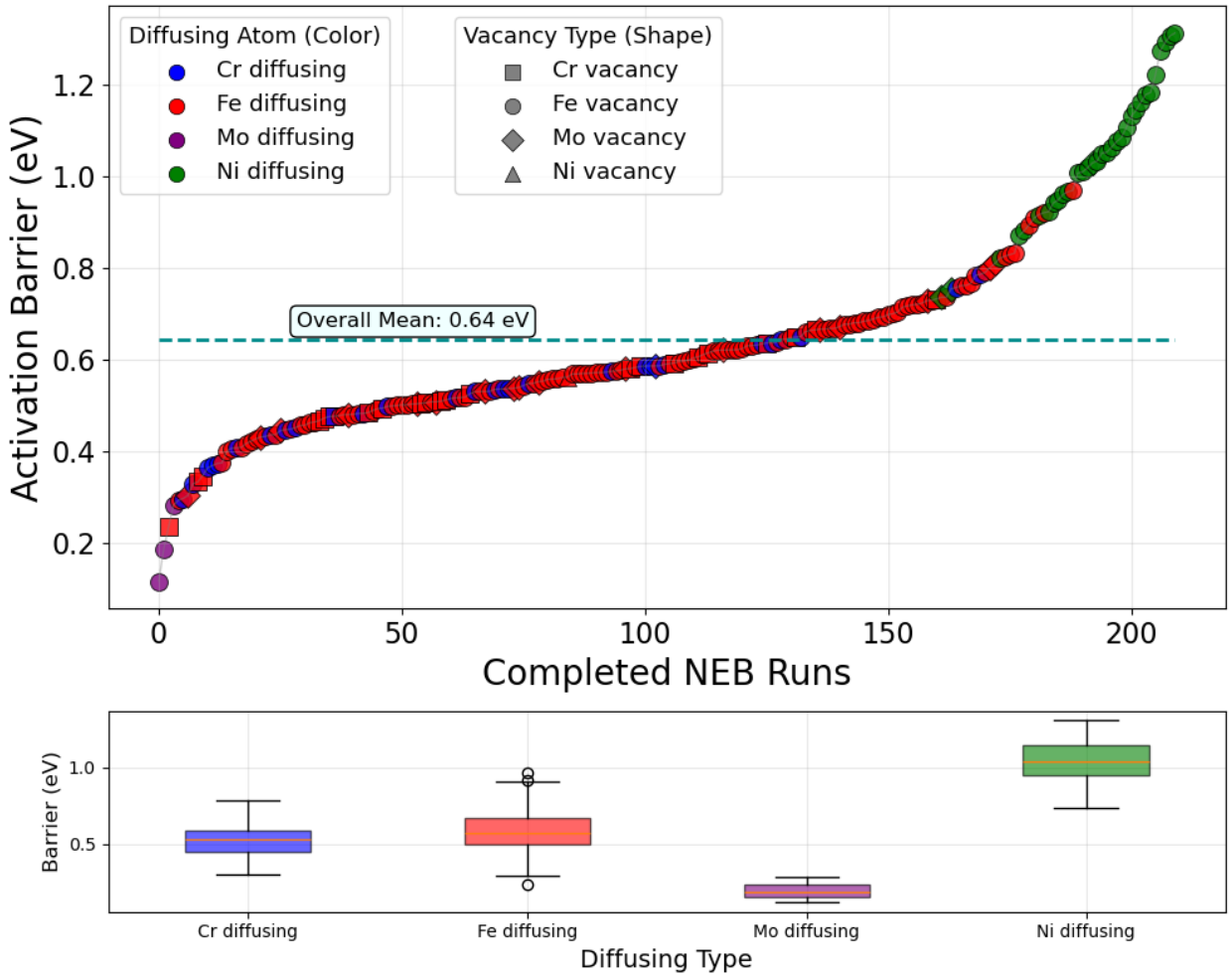

Figure 5. Activation barrier analysis showing (top) sorted distribution of all 210 calculated barriers colored by diffusing species and shaped by vacancy type, and (bottom) statistical distributions for each diffusing species. The sorted plot shows clear species separation for Mo and Ni, and significant overlap between Fe and Cr. The overall mean (0.64 eV, dashed line) falls between Fe and Cr distributions. Box plots reveal the species hierarchy: Mo << Cr ≈ Fe << Ni, with mean barriers ranging from 0.19 eV (Mo) to 1.05 eV (Ni). Scatter within each species reflects local chemical environment effects, validating the statistical sampling approach.

3.2 Species-Specific Diffusion Behavior

The calculated barriers show clear species-dependent trends that align with established understanding of diffusion in austenitic alloys, with one notable exception. When grouped by diffusing atom type, the barriers exhibit the following hierarchy:

Nickel diffusion shows consistently high activation barriers, with values ranging from 0.74 to 1.31 eV (mean: 1.045 ± 0.149 eV, n=32). This represents the slowest diffusion among all species studied and agrees with experimental observations that Ni is the slowest-diffusing major component in austenitic stainless steels. The substantial sample size provides high confidence in this behavior.

Iron diffusion exhibits moderate barriers spanning 0.23 to 0.97 eV (mean: 0.587 ± 0.127 eV, n=146), representing the most extensively sampled category due to Fe being the majority component. The broad distribution reflects the variety of local environments encountered by Fe atoms in the concentrated alloy, while the large sample size provides excellent statistical confidence.

Chromium diffusion produces barriers in the range of 0.30 to 0.79 eV (mean: 0.522 ± 0.117 eV, n=29), showing slightly faster diffusion than Fe on average. This modest difference suggests similar diffusion mechanisms for these two species, consistent with their similar atomic sizes and electronic properties.

Molybdenum diffusion shows remarkably low barriers of 0.12 to 0.28 eV (mean: 0.194 ± 0.068 eV, n=3). While the sample size remains limited, these exceptionally low barriers suggest that Mo atoms are highly mobile in the 316 SS matrix, potentially much faster than any other major alloying element. The tight distribution of Mo barriers despite different local environments provides confidence in this finding and has significant implications for understanding precipitation kinetics and phase evolution in 316 stainless steel.

3.3 Vacancy Environment Effects

The chemical identity of the vacancy site influences diffusion barriers, though the effects are modest compared to diffusing species identity, as shown in the vacancy environment matrix in Figure 6. Fe atom diffusion varies depending on the vacancy type: diffusion into Fe vacancies averages 0.60 eV, while diffusion into Cr vacancies averages 0.52 eV, into Ni vacancies averages 0.56 eV, and into Mo vacancies averages 0.57 eV. More substantial vacancy effects appear for other diffusion processes. Ni diffusion shows barriers averaging 0.84 eV when diffusing into Mo vacancies compared to 1.07 eV into Fe vacancies, representing a meaningful reduction of ~0.2 eV while Ni diffusion remains slow overall. The single observation of Cr-Cr self-diffusion (0.48 eV) falls within the expected range based on Fe-Cr and Fe-Fe barriers.

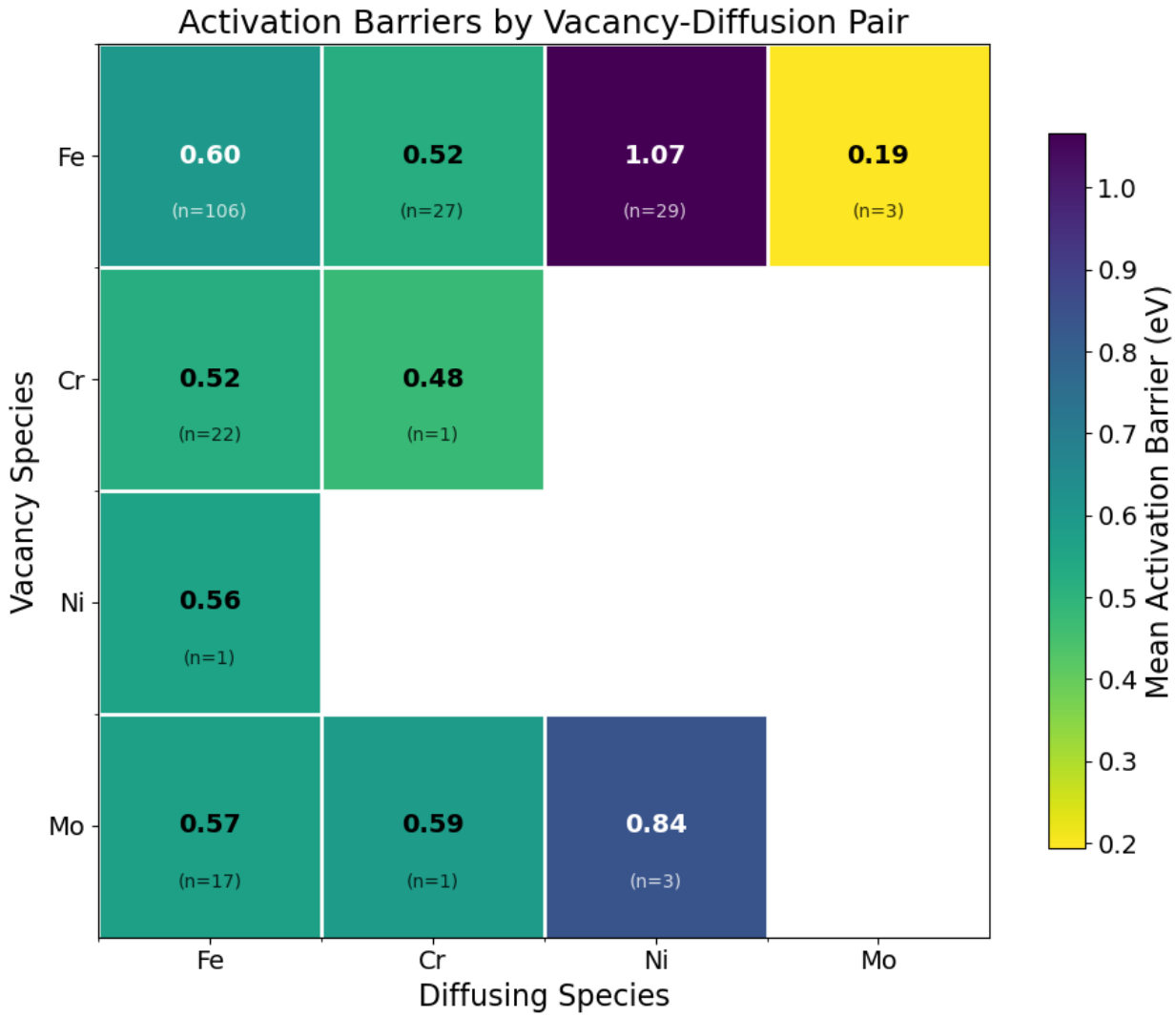

Figure 6. Vacancy environment matrix showing mean activation barriers for different vacancy-diffusion combinations in 316 stainless steel. Each cell displays the mean barrier (eV) with sample size in parentheses, colored by barrier magnitude (darker = higher barriers). The matrix demonstrates that diffusion barriers depend primarily on the diffusing species (columns) with secondary effects from vacancy type (rows). Diffusing Fe and Cr show similar activation barriers regardless of vacancy species. Diffusing Ni shows a notable drop in activation barrier when the vacancy species is Mo, though still higher than the barrier for other diffusing species. Sample sizes reflect the statistical distribution of defect configurations across different local chemical environments.

3.4 Composition Independence and Transferability

Activation barrier values are generally quite similar between the three compositional variants considered, as shown in Figure 7. This suggests that local chemical environment effects dominate over bulk composition changes in the 316 SS specification range. This finding supports the transferability of the calculated parameters to different 316 SS compositions and

validates the use of mean barriers for mesoscale modeling applications where composition-specific parameters may not be practical.

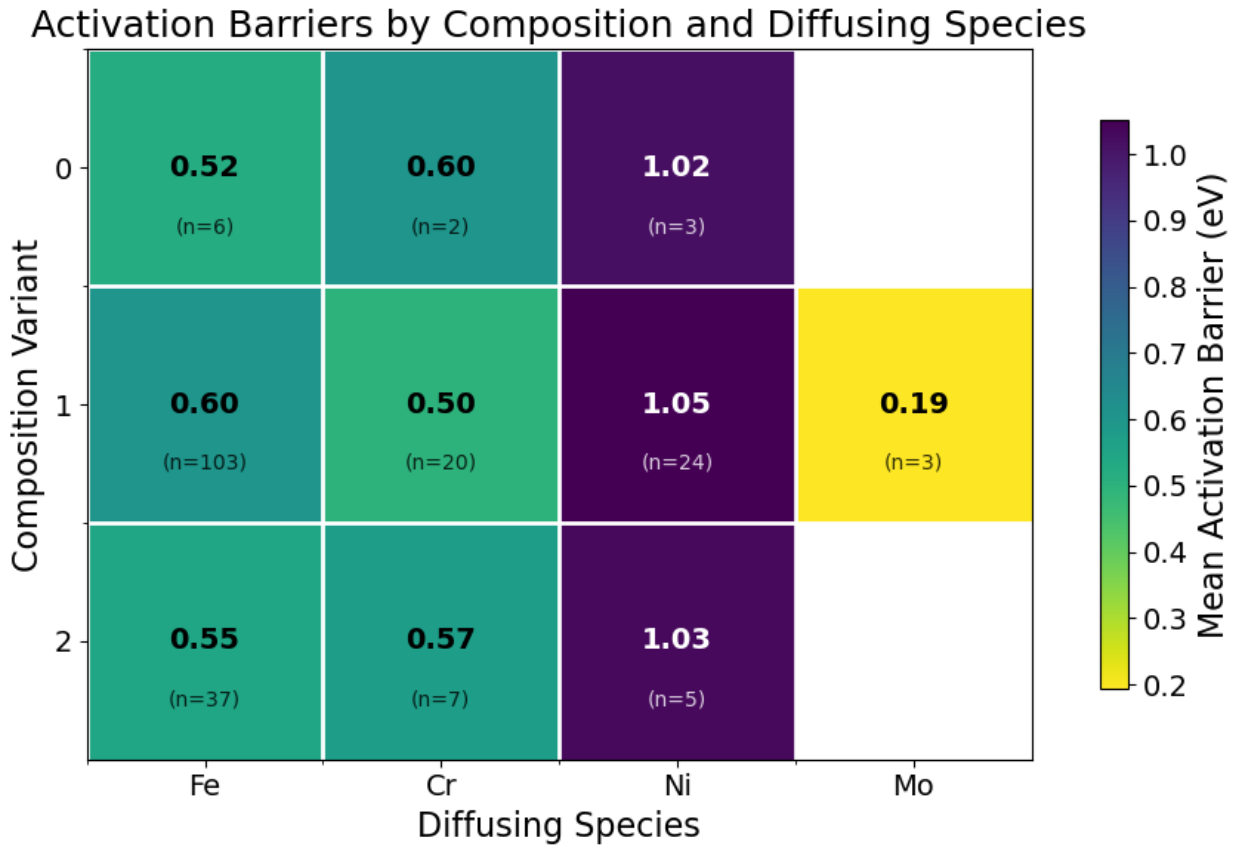

Figure 7. Composition dependence matrix showing mean activation barriers for different diffusing species across three 316 stainless steel composition variants. Each cell displays the mean barrier (eV) with sample size in parentheses, colored by barrier magnitude (darker = higher barriers). Composition 0 is the initial test composition, while Compositions 1 and 2 span the high and low ends of the Cr/Ni content range in 316 SS specification.

3.5 Comparison with Literature and Validation

The calculated species hierarchy (Ni >> Fe ≈ Cr >> Mo) agrees well with established trends for Fe, Cr, and Ni from both experimental measurements (Rothman, Nowicki, and Murch 1980; Assassa and Guiraldenq 1978) and previous DFT studies of simpler Fe-Ni and Fe-Cr-Ni systems (Klaver, Hepburn, and Ackland 2012; Fisher et al. 2025), though the barrier for Cr is generally a bit lower than Fe. The absolute values align well with previous DFT studies, which report migration barriers around 1.0–1.3 eV for Ni and 0.8–0.9 eV for Fe in Fe-Ni alloys (Fisher et al. 2025).

The systematic nature of these results for Fe, Cr, and Ni provides confidence in the computational methodology. The calculated barriers for Mo represent new theoretical predictions for this important alloying element, suggesting that Mo may play a more dynamic role in 316 SS microstructure evolution than previously recognized. The exceptionally low Mo barriers (0.12–0.28 eV) are unprecedented in the literature (to our knowledge) and suggest

rapid Mo mobility that could significantly affect precipitation kinetics, segregation behavior, and phase stability during thermal processing.

3.6 Implications for Phase Field Modeling

The activation barriers calculated in this work provide essential input parameters for mesoscale phase field simulations of microstructure evolution in 316 stainless steel. For phase field models requiring average diffusion parameters, the overall mean barrier of 0.61 eV represents a reasonable single-parameter approximation. However, the clear species-specific differences suggest that more sophisticated models could benefit from differentiated treatment.

The hierarchy of barriers (Ni >> Fe ≈ Cr >> Mo) indicates that Ni will be the rate-limiting species for many diffusion-controlled processes, while Mo's exceptionally high mobility could drive rapid local redistribution and affect precipitation kinetics. For phase field simulations of precipitate evolution, the fast Mo diffusion (barriers of 0.12–0.28 eV) suggests that Mo-rich phases may nucleate and grow more rapidly than expected from models using average diffusion parameters.

The statistical distributions of barriers within each species category also provide insight into local environment effects that could be incorporated into composition-dependent diffusion coefficients. The standard deviations (±0.068 to ±0.149 eV within species) represent meaningful variations that could affect predicted microstructure evolution timescales.

4.0 Conclusions

This work presents a systematic approach for calculating vacancy-mediated diffusion barriers in 316 stainless steel using density functional theory methods. The statistical sampling strategy, employing 210 NEB calculations across different local chemical environments, successfully addresses the challenges of chemical disorder in concentrated alloys and provides robust parameters for mesoscale modeling applications.

The computational methodology developed here demonstrates several important advances for complex alloy studies. The two-stage relaxation protocol with consistent magnetic treatment throughout all calculation stages proves essential for obtaining physically reasonable barriers. The systematic approach to convergence testing and validation establishes computational parameters that balance accuracy with efficiency for high-throughput calculations. Most importantly, the statistical sampling across multiple structural arrangements captures the effects of local chemical environments that are critical in concentrated alloys but often overlooked in smaller-scale DFT studies.

The calculated activation barriers reveal clear species-specific diffusion behavior that validates established trends while providing new insights into Mo mobility. The hierarchy Ni >> Fe ≈ Cr >> Mo confirms experimental observations that Ni is the slowest-diffusing major component, with barriers averaging 1.045 eV compared to 0.587 eV for Fe and 0.522 eV for Cr. The finding that Mo exhibits exceptionally low barriers (0.12–0.28 eV) represents a potentially significant discovery for understanding 316 SS microstructure evolution, suggesting that Mo redistribution may occur much more rapidly than previously recognized.

The consistency of barrier ranges across different compositions within the 316 SS specification demonstrates that the parameters are transferable and suitable for general use in mesoscale models. The overall mean barrier of 0.64 eV provides a practical single-parameter approximation, while the species-specific values enable more sophisticated treatments of diffusion-controlled processes. The statistical distributions also quantify the uncertainty associated with local environment effects, providing guidance for sensitivity analyses in larger-scale simulations.

This systematic approach is readily extensible to other multicomponent alloy systems where diffusion parameters are needed for mesoscale modeling but experimental data are limited. The methodology provides a pathway for generating the detailed material parameters required by modern computational materials science while maintaining the statistical rigor needed to account for chemical disorder effects. For 316 stainless steel specifically, these results provide the first comprehensive set of species-specific diffusion barriers suitable for predictive modeling of microstructure evolution processes including precipitation, grain boundary migration, and phase stability during thermal processing.

5.0 References

Ångqvist, Mattias, William A Muñoz, J Magnus Rahm, Erik Fransson, Céline Durniak, Piotr Rozyczko, Thomas H Rod, and Paul Erhart. 2019. "ICET–a Python library for constructing and sampling alloy cluster expansions." *Advanced Theory and Simulations* 2 (7): 1900015.

Arunkumar, J, S Abhaya, R Rajaraman, G Amarendra, KGM Nair, CS Sundar, and Baldev Raj. 2009. "Defect recovery in proton irradiated Ti-modified stainless steel probed by positron annihilation." *Journal of nuclear materials* 384 (3): 245-248.

Assassa, W, and P Guiraldenq. 1978. "Bulk and grain boundary diffusion of 59Fe, 51Cr, and 63Ni in austenitic stainless steel under influence of silicon content." *Metal Science* 12 (3): 123-128.

Davis, Joseph R. 1994. *ASM specialty handbook: stainless steels*. ASM.

Fisher, Adam M, Christopher D Woodgate, Xiaoyu Zhang, George C Hadjipanayis, Laura H Lewis, and Julie B Staunton. 2025. "Lattice vacancy migration barriers in Fe-Ni alloys, and why Ni atoms diffuse slowly: An ab initio study." *arXiv preprint arXiv:2508.19124*.

Georg, Kresse, Kresse Georg, J. Furthmüller, Furthmüller Jürgen, and Furthmüller Jürgen. 1996. "Efficient iterative schemes for ab initio total-energy calculations using a plane-wave basis set." *Physical Review B*. https://doi.org/10.1103/physrevb.54.11169. https://pubmed.ncbi.nlm.nih.gov/9984901.

Henkelman, Graeme, and Hannes Jónsson. 2000. "Improved tangent estimate in the nudged elastic band method for finding minimum energy paths and saddle points." *The Journal of chemical physics* 113 (22): 9978-9985.

Henkelman, Graeme, Blas P Uberuaga, and Hannes Jónsson. 2000. "A climbing image nudged elastic band method for finding saddle points and minimum energy paths." *The Journal of chemical physics* 113 (22): 9901-9904.

Klaver, TPC, DJ Hepburn, and GJ Ackland. 2012. "Defect and solute properties in dilute Fe-Cr-Ni austenitic alloys from first principles." *Physical Review B—Condensed Matter and Materials Physics* 85 (17): 174111.

Kresse, Georg, and Daniel Joubert. 1999. "From ultrasoft pseudopotentials to the projector augmented-wave method." *Physical review b* 59 (3): 1758. https://doi.org/10.1103/PhysRevB.59.1758. https://doi.org/10.1103/PhysRevB.59.1758.

Li, Yulan, Shenyang Hu, Xin Sun, and Marius Stan. 2017. "A review: applications of the phase field method in predicting microstructure and property evolution of irradiated nuclear materials." *npj Computational Materials* 3 (1): 16.

Liu, Xueyan, Hongwei Li, and Mei Zhan. 2018. "A review on the modeling and simulations of solid-state diffusional phase transformations in metals and alloys." *Manufacturing Review* 5: 10.

Mehrer, Helmut. 2007. *Diffusion in solids: fundamentals, methods, materials, diffusion-controlled processes*. Springer.

Perdew, John P, Kieron Burke, and Matthias Ernzerhof. 1996. "Generalized gradient approximation made simple." *Physical review letters* 77 (18): 3865. https://doi.org/10.1103/PhysRevLett.77.3865.

Ponga, Mauricio, Mohamed Hendy, Okan K Orhan, and Swarnava Ghosh. 2022. "Effects of the local chemical environment on vacancy diffusion in multi-principal element alloys." *arXiv preprint arXiv:2209.04010*.

Rothman, SJ, LJ Nowicki, and GE Murch. 1980. "Self-diffusion in austenitic Fe-Cr-Ni alloys." *Journal of Physics F: Metal Physics* 10 (3): 383.

Stukowski, Alexander. 2009. "Visualization and analysis of atomistic simulation data with OVITO–the Open Visualization Tool." *Modelling and simulation in materials science and engineering* 18 (1): 015012.

Xi, Zhucong, Mingfei Zhang, Louis G Hector Jr, Amit Misra, and Liang Qi. 2022. "Mechanism of local lattice distortion effects on vacancy migration barriers in fcc alloys." *Physical Review Materials* 6 (7): 073601.

Zunger, Alex, S-H Wei, Luiz G Ferreira, and James E Bernard. 1990. "Special quasirandom structures." *Physical review letters* 65 (3): 353.

Pacific Northwest National Laboratory

902 Battelle Boulevard
P.O. Box 999
Richland, WA 99354

1-888-375-PNNL (7665)

www.pnnl.gov